

# A Compton-thick nucleus in the dual AGN of Mrk 266

K. Iwasawa<sup>1,2</sup>, C. Ricci<sup>3,4,5</sup>, G. C. Privon<sup>6,7</sup>, N. Torres-Albà<sup>8</sup>, H. Inami<sup>9</sup>, V. Charmandaris<sup>10,11</sup>, A. S. Evans<sup>6,12</sup>,  
J. M. Mazzarella<sup>13</sup>, and T. Díaz-Santos<sup>3,14,11</sup>

<sup>1</sup> Institut de Ciències del Cosmos (ICCUB), Universitat de Barcelona (IEEC-UB), Martí i Franquès, 1, 08028 Barcelona, Spain

<sup>2</sup> ICREA, Pg. Lluís Companys 23, 08010 Barcelona, Spain

<sup>3</sup> Núcleo de Astronomía de la Facultad de Ingeniería y Ciencias, Universidad Diego Portales, Av. Ejército Libertador 441, Santiago, Chile

<sup>4</sup> Kavli Institute for Astronomy and Astrophysics, Peking University, Beijing 100871, China

<sup>5</sup> Department of Physics and Astronomy, George Mason University, MS 3F3, 4400 University Drive, Fairfax, VA 22030, USA

Department of Astronomy, University of Florida, 211 Bryant Space Sciences Center, Gainesville, FL 32611, USA

<sup>6</sup> National Radio Astronomy Observatory, 520 Edgemont Road, Charlottesville, VA 22903, USA

<sup>7</sup> Department of Astronomy, University of Florida, P.O. Box 112055, Gainesville, FL 32611, USA

<sup>8</sup> Department of Physics and Astronomy, Clemson University, Kinard Lab of Physics, Clemson, SC 29634, USA

<sup>9</sup> Hiroshima Astrophysical Science Center, Hiroshima University, 1-3-1 Kagamiyama, Higashi-Hiroshima, Hiroshima 739-8526, Japan

<sup>10</sup> Department of Physics, University of Crete, GR-71003 Heraklion, Greece

<sup>11</sup> Institute of Astrophysics, Foundation for Research and Technology—Hellas, Heraklion, GR-70013, Greece

<sup>12</sup> Department of Astronomy, University of Virginia, P.O. Box 400325, Charlottesville, VA 22904, USA

<sup>13</sup> IPAC, MC 100-22, California Institute of Technology, Pasadena, CA, 91125, USA

<sup>14</sup> Chinese Academy of Sciences South America Center for Astronomy, National Astronomical Observatories, CAS, Beijing 100101, China

November 15, 2021

## ABSTRACT

We present results of our analysis of *NuSTAR* data of the luminous infrared galaxy Mrk 266, which contains two nuclei, SW and NE, resolved in previous *Chandra* imaging. Combining with the *Chandra* data, we interpret the hard X-ray spectrum obtained from a *NuSTAR* observation as resulting from steeply rising flux from a Compton-thick AGN in the SW nucleus which is very faint in the *Chandra* band, confirming the previous claim of Mazzarella et al. (2012). This hard X-ray component is dominated by reflection, and its intrinsic 2-10 keV luminosity is likely to be  $\sim 1 \times 10^{43}$  erg s<sup>-1</sup>. Although it is bright in soft X-ray, only moderately absorbed NE nucleus has a 2-10 keV luminosity of  $4 \times 10^{41}$  erg s<sup>-1</sup>, placing it in the low-luminosity AGN class. These results have implications for understanding the detectability and duty cycles of emission from dual AGN in heavily obscured mergers.

**Key words.** X-rays: galaxies - Galaxies: active - Galaxies:individual (Mrk 266)

## 1. Introduction

Mrk 266 (= NGC5256) is a major merger of two galaxies with nearly equal masses with a nuclear separation of 10 arc-sec, corresponding to a projected physical distance of 6 kpc at  $z = 0.0279$ . It is a luminous infrared galaxy (LIRG) with  $L_{8-1000\mu\text{m}} = 3.6 \times 10^{11} L_{\odot}$ , and is a member of the Great Observatories All-sky LIRG Survey (GOALS, Armus et al. 2009). While a significant portion of the large IR luminosity originates in intense star formation, both galaxies host active galactic nuclei (AGN). Dual AGN in galaxy mergers are relatively rare in infrared-selected samples like GOALS (four out of 54 multiple systems, Iwasawa et al. 2011; Torres-Albà et al. 2018; Iwasawa et al. 2018), likely due to heavy obscuration making them difficult to detect rather than their absence. Mrk 266 provides a good opportunity for a detailed study of dual AGN in a luminous IR system. The two AGN, as described in this paper, are, however, found to have rather different characteristics despite their similar host galaxy masses, and heavy obscuration indeed plays a significant role.

Following on the extensive multiwavelength analysis of Mrk 266 presented by Mazzarella et al. (2012, hereafter MIV12),

here we give a brief summary of known properties focusing on the two active nuclei residing in the south-western (SW) and north-eastern (NE) galaxies. The galaxies have comparable masses around  $(5-6) \times 10^{10} M_{\odot}$ , from which the black hole mass of each nucleus is estimated to be  $\sim 2 \times 10^8 M_{\odot}$ , based on their bulge luminosities (Marconi & Hunt 2003). The individual galaxies have  $L_{\text{IR}}$  of  $2.3 \times 10^{11} L_{\odot}$  (SW) and  $0.7 \times 10^{11} L_{\odot}$  (NE). This seems to be compatible with the Herschel imaging at 70  $\mu\text{m}$  and 100  $\mu\text{m}$ , which marginally resolves them (Chu et al. 2017). While there is a confusion arising from reversed classifications given in literature, the most likely optical classifications of the SW and NE nuclei are Seyfert 2 and LINER, respectively, as supported by works either dedicated to Mrk 266 or on small samples including Mrk 266 (Osterbrock & Dahari 1983; Kollatschny & Fricke 1984; Hutchings et al. 1988; Mazzarella & Boroson 1993; Osterbrock & Martel 1993; Wang et al. 1997; Wu et al. 1998; Ishigaki et al. 2000). The mid-IR spectroscopy with the Spitzer IRS, as summarised by MIV12 (references are therein), show that the spectra of both nuclei are dominated by polycyclic aromatic hydrocarbon (PAH) emission, indicating an intense starburst. However, presence of AGN is also suggested

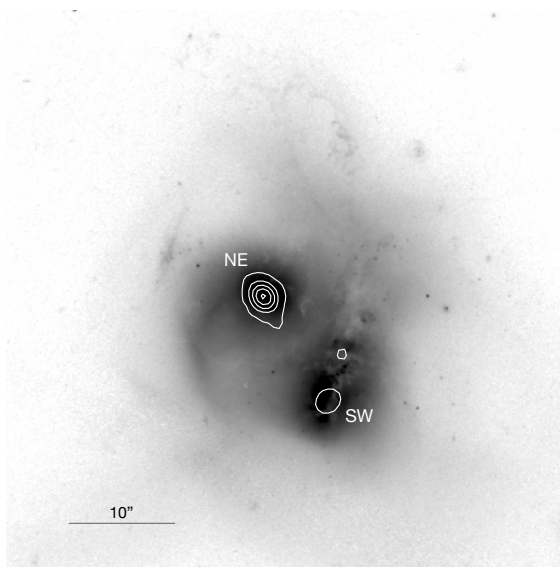


Fig. 1: HST ACS/WFC image of Mrk 266 obtained with the F814W filter, overlaid by Chandra 4-7 keV image contours. The five contour levels are linearly spaced between 0.15 to 3.8 counts pixel<sup>-1</sup>. North is up, east to the left. The SW and NE nuclei are labelled. The scale bar of 10 arcsec is shown.

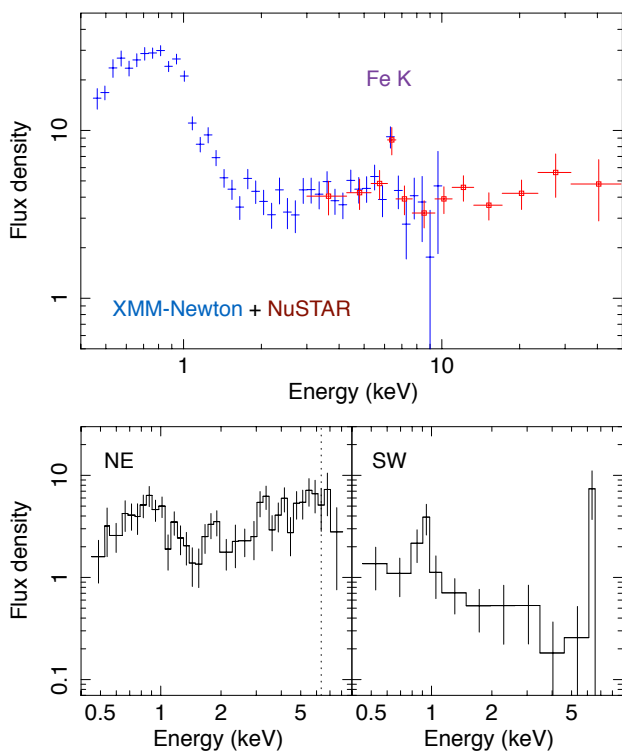


Fig. 2: Upper panel: Flux density spectrum of integrated emission of Mrk 266, containing both NE and SW nuclei. Data from XMM-Newton (blue) and NuSTAR (red squares) are plotted. The flux density is in units of  $10^{-14}$  erg s<sup>-1</sup> cm<sup>-2</sup> keV<sup>-1</sup>. For displaying purpose, the NuSTAR data used for the spectral analysis are rebinned further. Fe K emission line feature at 6.5 keV is marked. Bottom panel: Spectra of the NE and SW nuclei obtained from the Chandra ACIS. Since Fe K line emission is absent in the NE spectrum (the line energy is denoted by the vertical dotted line), the Fe K line seen in the XMM-Newton and NuSTAR spectra seems to originate predominantly from SW.

by high-ionization lines such as [Ne v] $\lambda$ 14.3, 24.3 $\mu$ m, and [O iv] $\lambda$ 25.9 $\mu$ m for SW, and warm dust continuum for NE (see also Imanishi et al. 2009). A Chandra observation, which resolves the two nuclei, shows that a hard-spectrum source is clearly seen at NE (Fig. 1), supporting the presence of a moderately obscured AGN with  $N_{\text{H}} = (7 \pm 2) \times 10^{22}$  cm<sup>-2</sup> (Brassington et al. 2007; MIV12; Torres-Albà et al. 2018). On the other hand, SW is  $\sim 13$  times fainter than NE and barely detected in the Chandra hard-band (4-7 keV) image (Fig. 1). SW is also fainter than NE in optical/UV but becomes progressively brighter at longer wavelengths  $\geq 3\mu$ m, leading to SW to be  $\sim 3$  times more luminous than NE in the whole IR band. The molecular gas mass in SW is estimated to be  $M(\text{H}_2) = 3.4 \times 10^9 M_{\odot}$ , which is  $\sim 5$  times larger than that of NE (Imanishi et al. 2009, these are measurements obtained from interferometric observations but are consistent with a single-dish measurement by Sanders et al. 1986). These characteristics suggest that obscuration might be responsible for the relative faintness of the SW nucleus in X-rays. The XMM-Newton spectrum of Mrk 266, which does not resolve the individual galaxies, shows a strong Fe K line (MIV12). No Fe K line is present in the Chandra spectrum of NE, but in the spectrum of SW (the Fe K line is, in fact, the major source of 4-7 keV counts detected with Chandra). This led MIV12 to suspect that SW contains a Compton-thick AGN, in which the direct X-ray continuum is totally suppressed in the Chandra bandpass and only the Fe K line in its reflected light is observed. It is reminiscent of the double nucleus in another merger system in GOALS, Mrk 273, in which a Compton-thick nucleus is inferred for the northern nucleus which is molecular-rich, and the major IR source of the merger system (e.g. U et al. 2013; Iwasawa et al. 2011, 2018; Liu et al. 2019). In this paper, we examine this hypothesis for Mrk 266 using new NuSTAR data which cover the 3-50 keV band, expecting a sharp rise of X-ray flux of SW above 10 keV which would exceed the flux from NE in the NuSTAR band.

The cosmology adopted here is  $H_0 = 70$  km s<sup>-1</sup> Mpc<sup>-1</sup>,  $\Omega_{\Lambda} = 0.72$ ,  $\Omega_{\text{M}} = 0.28$ .

## 2. Observations

Mrk 266 was observed with NuSTAR, XMM-Newton and Chandra X-ray Observatory and the observation log is shown in Table 1. The NuSTAR data were taken as part of The NuSTAR Obscured Seyferts Survey (PI: J. Miller) and we retrieved the data from the public archive. We used the event file processed by the standard pipeline. Spectral data extracted from a circular aperture with a radius of 30'' of the two Focal Plane Modules, FPMA and FPMB, were combined for the analysis presented below. The spectral data of the two modules agree to each other within statistical error, and the low-energy effective area problem reported for FPMA (Madsen et al. 2020) seems to have little impact. Since the NE and SW nuclei are unresolved with the NuSTAR beam, the spectrum contains emission from both nuclei, as in the XMM-Newton spectrum. The spectral data obtained from XMM-Newton and Chandra are the same as those presented in MIV12.

## 3. Results

The NuSTAR spectrum agrees with the XMM-Newton EPIC spectrum in the overlapping 3-10 keV band, both in continuum and Fe K line (Fig. 2). The 3-50 keV NuSTAR spectrum can be well described by a power-law of energy index

Table 1: X-ray observations of Mrk 266.

Observatory	Date	ObsID	Exposure	Counts	Band
Chandra	2001-11-02	2044	20	124	3-8 keV
XMM-Newton	2002-05-15	0055990501	13/18	562	3-10 keV
NuSTAR	2019-02-08	60465005002	64	441	3-50 keV

**Notes.** The ‘Exposure’ column shows useful exposure time in each observation in units of  $10^3$  seconds. The ‘Counts’ column gives background-corrected source counts in the energy band shown in the following column. The two exposure times shown for the XMM-Newton observation are of the EPIC pn and the two EPIC MOS cameras. The source counts for XMM-Newton and NuSTAR are sums of the three EPIC cameras and two FPMs, respectively.

$\alpha = 0.0 \pm 0.1^1$  plus a narrow Gaussian line at  $6.5 \pm 0.1$  keV for Fe K ( $\chi^2 = 46.0$  for 51 degrees of freedom). The Fe line intensity is  $(2.9 \pm 1.0) \times 10^{-6}$  ph cm $^{-2}$  s $^{-1}$ , corresponding to EW =  $0.80 \pm 0.27$  keV.

A hard spectrum with a slope as observed at lower energies would be interpreted as evidence of moderate absorption of  $N_{\text{H}} \leq 10^{23}$  cm $^{-2}$ , as an intrinsic AGN spectrum is known to have a well defined range of slope around  $\alpha = 0.8$  with a standard deviation of 0.15 (e.g. Ueda et al. 2014; Nandra & Pounds 1994). The measured spectral slope,  $\alpha \approx 0.0$ , stretching up to 50 keV, is however unusual, because a spectral slope would start to approach the intrinsic value towards higher energies as the effect of such moderate absorption diminishes. Therefore it is unlikely that a single source, that is the NE nucleus, dominates the NuSTAR bandpass as it does in the 4-7 keV Chandra image. Instead, the NuSTAR spectrum strongly suggests, besides the NE source, a presence of an extra component rising above the Chandra bandpass to elevate the hard band continuum emission. This is the same line of argument used to convey the presence of a Compton-thick AGN in the northern nucleus of Mrk 273 using NuSTAR data (Iwasawa et al. 2018). As argued in MIV12, SW is a likely source of this extra hard component which can be attributed to a Compton-thick AGN.

According to the above hypothesis, we model the NuSTAR spectrum with two components from NE and SW. To avoid overfitting, we tested the two-component model leaving a minimum set of parameters free. Many model parameters were set to be reasonable or known values. A first assumption is that both X-ray sources in NE and SW have the identical, standard AGN slope of  $\alpha = 0.9$ . This is the intrinsic slope of the power-law source, not the apparent slope of  $\alpha = 0.8$  mentioned above, which is affected by a contribution of reflection from a surrounding medium, e.g. Nandra & Pounds (1994).

The NE spectrum is mildly absorbed. The absorbing column density is found to be  $N_{\text{H}} = (6.8 \pm 3.8) \times 10^{22}$  cm $^{-2}$ , by fitting the Chandra NE spectrum and we adopted the best-fit  $N_{\text{H}}$ . This leaves the normalization of the power-law as the only free parameter for the NE component.

The SW component is of our primary interest. However, as shown below, various configurations of a Compton-thick torus can describe the NuSTAR spectrum of the present quality, as long as  $N_{\text{H}} \geq 2 \times 10^{24}$  cm $^{-2}$  is met. Therefore we tested two modelling options for a Compton-thick AGN: *SW-A*: a strongly absorbed spectrum; and *SW-R*: a reflection-dominated spectrum. In both cases, we use *etorus* (Ikeda et al. 2009; Awaki et al. 2009), one of the Monte-Carlo codes to compute X-ray spectra emerging from an X-ray source surrounded by an absorber with a torus geometry, including Compton-scattered light. The

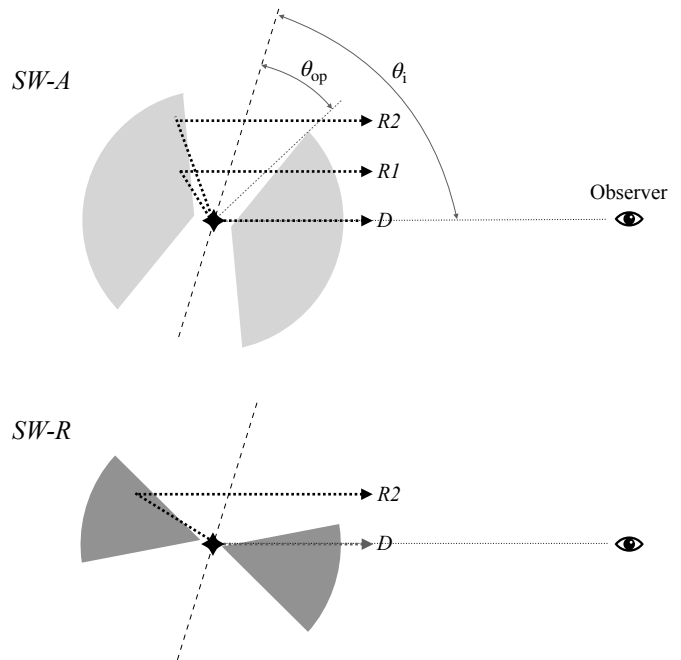


Fig. 3: Cross-section view of X-ray absorbing torus configurations assumed for the absorption-dominated (*SW-A*) and reflection-dominated (*SW-R*) models. The torus parameters of *etorus* given in Table 2 are illustrated. The inclination angle and half-opening angle are denoted as  $\theta_i$  and  $\theta_{\text{op}}$ . *D*, *R1* and *R2* represent direct light from the central X-ray source penetrating through the absorbing column in the line of sight, reflected light coming off from the part of the inner surface of the torus, hidden from the direct view (“Reflection 1” as defined in Ikeda et al. (2009)), and reflected light coming from the visible inner surface (“Reflection 2”), respectively. In *SW-A*, an observed spectrum is dominated by *D* and weaker *R1*, which has practically the same spectral shape as *D*. In *SW-R*, *R2*, which has a Compton-scattered low-energy tail, is the dominant component, since *D* (and a minor *R1* contribution) is strongly suppressed by the large optical depth in the line of sight.

*etorus* offers flexible parameterisations of torus geometry similar to those in another recent code *borus02* (Baloković et al. 2018), and Baloković et al. (2018) reported that the two codes produce well-matched reflection spectra, apart from fluorescent emission-lines, which are not included in the current version of *etorus*. We model the most prominent Fe K line by a narrow Gaussian. The torus parameters were chosen so that a resulting model gives a representative spectral shape for each option. They are illustrated in Fig. 3. See Figures 3 and 4 of Ikeda et al. (2009) for visualization of the simulated spectral components. Since

<sup>1</sup> We use energy-index  $\alpha$  for a power-law spectral slope, as it is appropriate for flux density spectra shown in this article. It is related to the conventional photon index  $\Gamma$  by  $\Gamma = 1 + \alpha$ .

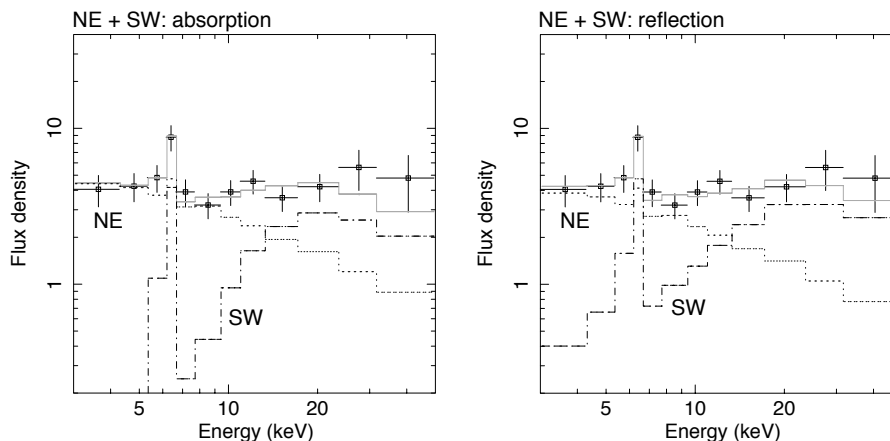


Fig. 4: The NuSTAR spectrum of Mrk 266 and the best-fitting two-component model (grey line): Left: *SW-A*; Right: *SW-R*. The contributions of the NE (dotted line) and SW (dash-dotted line) nuclei are overplotted. As same as in Fig. 2, the NuSTAR data used for the analysis are rebinned further for displaying purpose. Relative contributions of NE and SW change dramatically across the energy range.

Table 2: Two-component fits to the NuSTAR spectrum.

NE		
$N_{\text{H}}$	$6.8 \times 10^{22}$	
SW		
	<i>SW-A</i>	<i>SW-R</i>
$N_{\text{H}}$	$1.7^{+1.2}_{-0.6} \times 10^{24}$	$7 \times 10^{24}$
$\theta_{\text{op}}$	$30^\circ$	$70^\circ$
$\theta_{\text{i}}$	$72^\circ$	$72^\circ$
Fe K line		
$E$	$6.49 \pm 0.09$	$6.49 \pm 0.09$
$I$	$2.6 \pm 1.0$	$2.5 \pm 1.0$
$\chi^2/\text{dof}$	46.8/50	45.9/51

**Notes.** The 3-50 keV NuSTAR spectrum was fitted by NE and SW composite models with two modelling options for the SW component, 1) *SW-A*: absorption-dominated; and 2) *SW-R*: reflection-dominated spectrum. The spectral slope for both components are assumed to be  $\alpha = 0.9$ . The SW spectrum is computed by the torus spectrum model *etorus* (Ikeda et al. 2009). The torus configuration is determined by an opening angle,  $\theta_{\text{op}}$ , and inclination,  $\theta_{\text{i}}$ . Apart from the absorbing column for *SW-A*, free parameters are normalizations of the respective NE and SW continuum and the centroid energy and intensity of a Gaussian for Fe K line. The values of  $N_{\text{H}}$ , line energy ( $E$ ) and intensity ( $I$ ) are in units of  $\text{cm}^{-2}$ , keV, and  $10^{-6} \text{ ph cm}^{-2} \text{ s}^{-1}$ , respectively.

Table 3: Decomposed fluxes of the NE and SW nuclei.

Band	NE	SW
<i>SW-A</i>		
3-10 keV	2.4	0.15
10-30 keV	3.1	4.2
<i>SW-R</i>		
3-10 keV	2.1	0.45
10-30 keV	2.7	4.9

**Notes.** Fluxes for NE and SW components in 3-10 keV and 10-30 keV bands, obtained from the spectral decompositions of the NuSTAR data for the two spectral modelling options for SW, *SW-A* and *SW-R* (see text and Table 2). The fluxes are in units of  $10^{-13} \text{ erg s}^{-1} \text{ cm}^{-2}$ . The 3-10 keV flux for SW is for the continuum only and does not include the Fe K line flux which is  $0.24 \times 10^{-13} \text{ erg s}^{-1} \text{ cm}^{-2}$ .

the line-of-sight is obscured, the absorbing torus is expected to be highly inclined and we assume its inclination angle to be  $\theta_{\text{i}} = 72^\circ$  (approximately a middle value of the  $45^\circ$ - $90^\circ$  range). In *SW-A*, a relatively narrow torus-opening angle  $\theta_{\text{op}} = 30^\circ$  is assumed so that the inner surface of the torus is hardly visible and thus the observed spectrum is dominated by an absorbed component of the central source. The absorbing column and the power-law normalization are fitted. The absorbing column density is found to be  $N_{\text{H}} = 1.7^{+1.2}_{-0.6} \times 10^{24} \text{ cm}^{-2}$ . In *SW-R*, a wide opening angle  $\theta_{\text{op}} = 70^\circ$  and a large  $N_{\text{H}} = 7 \times 10^{24} \text{ cm}^{-2}$  are assumed, which results in a spectrum being reflection dominated, since the highly Compton-thick opacity assures that the direct light from the central source is strongly suppressed and has a negligible contribution to the observed spectrum whilst the wide  $\theta_{\text{op}}$  makes the torus inner wall well visible (but the central source still hidden from direct view by a small margin of  $\Delta\theta = 2^\circ$ ). The only free parameter is the power-law normalization.

These spectral modellings give good matches to the NuSTAR data with comparable quality, as shown in Fig. 4 and Table 2. The Fe K line EW is found to be  $\approx 0.6 \pm 0.23 \text{ keV}$  with respect to the total continuum. Note that depending on the SW modelling options, decomposed fluxes of NE and SW vary (Table 3).

The NuSTAR data cannot distinguish between *SW-A* and *SW-R*. The primary reason is that, although the spectral models for SW expected from *SW-A* and *SW-R* differ at some degree at energies below the Fe K band (see Fig. 4), this difference is compensated by varying normalization of the NE model. Here we investigate if the Chandra data of SW can tell the difference, albeit with low source counts. The Chandra data for SW have 6 counts in 3-7 keV (no counts at higher energies), and apart from the 4 counts for the Fe K line, 2 counts are detected in the 4-5 keV band. The *SW-A* model has a sharp decline below 6 keV and its expected count rate in 4-5 keV is  $5 \times 10^{-6} \text{ ct s}^{-1}$  while the *SW-R* model has a Compton-scattered tail towards lower energies giving an expected count rate of  $5 \times 10^{-5} \text{ ct s}^{-1}$ . The observed count rate  $1.0 \times 10^{-4} \text{ ct s}^{-1}$  lies closer to the latter. Among 1000 simulations of Chandra data based on the absorption model, there is null incidence of 2 or more counts in 4-5 keV, which, in contrast, occur 19% of simulations under the reflection model. This seems to favour the reflection model unless the 4-5 keV counts come from any other external sources, for example, X-ray binary emission from a starburst which cannot be ruled out.

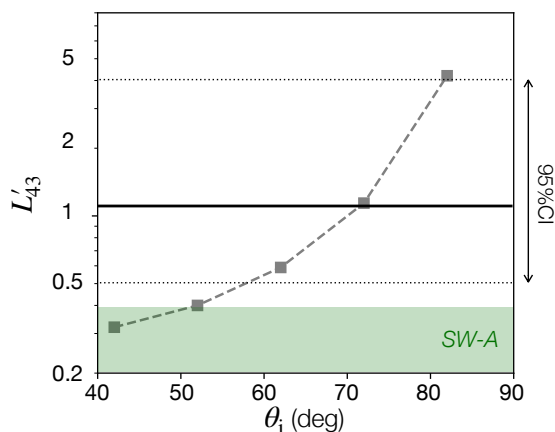


Fig. 5: Intrinsic 2-10 keV luminosity of the SW nucleus estimated for the reflection-dominated model *SW-R*, as a function of assumed inclination angle ( $\theta_i$ ) of the obscuring torus. The intrinsic luminosity,  $L'_{43}$ , is in units of  $10^{43}$  erg  $s^{-1}$ . For  $\theta_i = 42^\circ$ - $72^\circ$ ,  $\theta_i = \theta_{op} + 2^\circ$  is assumed. For the point for  $\theta_i = 82^\circ$ ,  $\theta_{op} = 70^\circ$  is used as it is the upper bound of the *etorus* model. The thick horizontal line indicates the best-estimate of  $L'_X = 1.3 \times 10^{43}$  erg  $s^{-1}$ , obtained by combining the X-ray and mid-IR feature based estimates (see Sect. 4.1) and the 95% CI is indicated by two dotted-lines. The  $L'_X$  value derived from the nominal *SW-A* model (see Table 2) is  $0.2 \times 10^{43}$  erg  $s^{-1}$ , i.e. the bottom of the panel, but could go up within the shaded area depending on an assumed geometry (see text) in the absorption model.

Estimating an intrinsic 2-10 keV luminosity,  $L'_X$ , of an absorbed X-ray source is straightforward when its absorption opacity is significantly smaller than a Thomson depth, or  $N_H \ll 10^{24}$   $cm^{-2}$ , for example, in the case of the NE X-ray source.  $L'_X(NE)$  is  $(3.8\text{--}4.4) \times 10^{41}$  erg  $s^{-1}$ , depending on the choice of spectral model for SW. In the Compton-thick regime, the absorption correction has dependency on an assumed torus geometry (Matt et al. 1999). This applies to the absorption-dominated model (*SW-A*) for SW. In our assumed torus geometry which has a large covering fraction (Table 2),  $L'_X(SW) = 2.0 \times 10^{42}$  erg  $s^{-1}$ . However, a similar absorption-dominated spectrum can be obtained with a smaller covering torus with, say,  $\theta_{op} = 70^\circ$  if the torus is precisely edge-on ( $\theta_i \simeq 90^\circ$ ). In this configuration, since less light is Compton-scattered into the line of sight from a small-covering torus than from that of large-covering, the (absorbed) illuminating source has to be more luminous, resulting in a factor of  $\sim 2$  larger  $L'_X(SW)$  of  $3.9 \times 10^{42}$  erg  $s^{-1}$ . This is a special configuration and it sets the upper bound of  $L'_X$  for *SW-A*.

Uncertainty in the intrinsic luminosity estimate is even larger when observed light is reflection-dominated as no direct light from the obscured source is visible. In the *SW-R* model,  $\theta_{op} = 70^\circ$  and  $\theta_i = 72^\circ$  are assumed, but as long as  $\theta_i = \theta_{op} + 2^\circ$  is maintained,  $\theta_{op} = 40^\circ$ - $70^\circ$  gives a similar quality of fit. However, since the visible surface of the torus inner wall becomes small as the torus inclination  $\theta_i$  increases (while the spectral shape of reflected light remains similar), the illuminating source needs to be more luminous to produce the same reflection luminosity and vice versa, as shown in Fig. 5. For  $\theta_i = 72^\circ$ , the intrinsic luminosity is estimated to be  $L'_X = 1.1 \times 10^{43}$  erg  $s^{-1}$ , but could be smaller if  $\theta_i$  is smaller. At a given  $\theta_i$ , decreasing  $\theta_{op}$  also makes the visible reflection surface smaller and thus pushes up the illuminating luminosity. However, too small  $\theta_{op}$  would loose the quality of fit for the NuSTAR data due to a mismatch in the Fe K

Table 4: AGN luminosities of NE and SW.

	$\log L'_X$	$\log L_{AGN}$	$\log \lambda_{Edd}$	$\log (L_{AGN}/L_{IR})$
NE	41.60	42.80	-3.68	-1.63
SW	43.13	44.43	-2.04	-0.51

**Notes.** The best-estimate of intrinsic 2-10 keV luminosity  $L'_X$  and X-ray based AGN bolometric luminosity  $L_{AGN}$  in units of erg  $s^{-1}$ , Eddington ratio  $\lambda_{Edd}$ , and the AGN luminosity and IR luminosity ratio for NE and SW nuclei. See text and Fig. 5 for the details of the estimates of  $L'_X$ , their uncertainties, and the bolometric corrections.

absorption edge depth (a small  $\theta_{op}$  results in a relative increase of reflection light coming through the torus over directly visible reflection leading to a deeper Fe K edge, which overestimates the observed edge depth). For  $\theta_i = 72^\circ$ , we obtain a constraint of  $\theta_{op} > 55^\circ$  (the 90% lower limit). By decreasing  $\theta_{op}$ , the data start to favour the absorption-dominated spectrum with smaller  $N_H$  towards that obtained in *SW-A*. Thus, although there is a small forbidden area in the parameter space, various combinations of the torus parameters are possible to describe the NuSTAR spectrum. Accordingly, the 2-10 keV intrinsic luminosity of the obscured nucleus in SW,  $L'_X(SW)$ , could range from  $2 \times 10^{42}$  erg  $s^{-1}$  to  $4 \times 10^{43}$  erg  $s^{-1}$ .

## 4. Discussion

Our analysis of the NuSTAR spectrum suggests that the SW nucleus contains a Compton-thick nucleus, which is intrinsically more luminous than the NE nucleus, as speculated by MIV12. Before examining their AGN properties in turn, some basic parameters of the two nuclei are summarised. The black hole masses for the two nuclei, estimated from their host spheroidal luminosities, are similarly  $M_{BH} = 2 \times 10^8 M_\odot$ , for which the Eddington luminosity is  $L_{Edd} \sim 3 \times 10^{46}$  erg  $s^{-1}$ . The infrared luminosity estimated for NE and SW nuclei are  $L_{IR}(NE) = 2.7 \times 10^{44}$  erg  $s^{-1}$ , and  $L_{IR}(SW) = 8.7 \times 10^{44}$  erg  $s^{-1}$ . The AGN bolometric luminosity estimated from X-ray  $L_{AGN} = \kappa L'_X$  where  $\kappa$  is the X-ray bolometric correction, Eddington ratio  $\lambda_{Edd}$ , and  $L_{AGN}/L_{IR}$  ratio for each nucleus, as discussed below, are given in Table 4.

### 4.1. SW nucleus

As shown in Sect. 3, SW is likely a Compton-thick AGN with  $N_H \geq 2 \times 10^{24}$   $cm^{-2}$ , but the intrinsic X-ray luminosity  $L'_X$  of the heavily obscured source remains uncertain between  $2 \times 10^{42}$  erg  $s^{-1}$  and  $4 \times 10^{43}$  erg  $s^{-1}$ . AGN-related mid-IR diagnostics seem to have a close relation to AGN bolometric power (e.g. Gruppioni et al. 2016). Since some of them have been reported to have a good correlation directly with intrinsic X-ray emission, we examine their predictions of  $L'_X$  below.

On account of being dust re-radiation from an obscuring torus, the mid-infrared continuum emission of AGN has been found to correlate tightly with the intrinsic 2-10 keV luminosity (Lutz et al. 2004; Horst et al. 2008; Gandhi et al. 2009; Mateos et al. 2015). However, one difficulty is to isolate an AGN component from other continuum sources at the same wavelength. In Mrk 266, the available mid-IR photometric data were obtained from apertures with  $>$  a few arcsec of the Spitzer-IRAC or IRAS, and we face the difficulty mentioned above. First, we directly adopt the available photometric data, which gives an upper limit on  $L'_X$ . From the SED given in Fig. 9 of MIV12, luminosities of SW at  $6 \mu m$  and  $12 \mu m$  are estimated to be  $L_6 = 4.2 \times 10^{43}$  erg  $s^{-1}$

and  $L_{12} = 1.0 \times 10^{44}$  erg s<sup>-1</sup>, respectively. Using the correlation for 6  $\mu\text{m}$  by Mateos et al. (2015),  $L'_X \approx 2 \times 10^{43} f_{\text{AGN}}$  erg s<sup>-1</sup> is obtained, where  $f_{\text{AGN}}$  denotes the AGN fraction at the mid-IR wavelength. Similarly, the correlation for 12  $\mu\text{m}$  of Gandhi et al. (2009) gives  $L'_X \approx 5 \times 10^{43} f_{\text{AGN}}$  erg s<sup>-1</sup>. We note that Mateos et al. (2015) and Gandhi et al. (2009) use distinct samples of AGN and their scaling-relations are calibrated independently. The AGN fraction,  $f_{\text{AGN}}$ , in SW is estimated by various mid-IR diagnostics (MIV12; Díaz-Santos et al. 2017) which, however, spread widely, likely due to aperture effects. Here, we tentatively adopt the median of the six diagnostics,  $f_{\text{AGN}} = 0.35$ , which yields  $L'_X$  estimates of  $0.7 \times 10^{43}$  erg s<sup>-1</sup> and  $1.7 \times 10^{43}$  erg s<sup>-1</sup>, based on  $L_6$  and  $L_{12}$ , respectively.

Another X-ray luminosity estimator is the [O iv]  $\lambda 25.9\mu\text{m}$  emission line, which also shows a tight correlation with  $L_X$  (Meléndez et al. 2008; Rigby et al. 2009; Diamond-Stanic et al. 2009; Liu et al. 2014). As [O iv] is a high-excitation line which is likely to arise from AGN irradiation, it should be largely free from external contamination (Pereira-Santaella et al. 2010), unlike the continuum emission, and thus directly scales with the AGN luminosity. Being a mid-IR line, it is also relatively robust against dust extinction. Therefore it is deemed to give a reliable estimate of the AGN intrinsic luminosity. The [O iv] flux measured with the IRS aperture containing only SW is available (MIV12; Bernard-Salas et al. 2009), which gives [O iv] luminosity of  $8 \times 10^{41}$  erg s<sup>-1</sup>. The [Oiv]- $L'_X$  correlation of Liu et al. (2014) for Seyfert 2 galaxies gives  $L'_X \approx 1.9 \times 10^{43}$  erg s<sup>-1</sup>.

The above three predictions of  $L'_X$  from the mid-IR features all lie around  $\sim 1 \times 10^{43}$  erg s<sup>-1</sup>, and within the range inferred by the modelling of the NuSTAR data. This supports the reflection-dominated spectrum of SW-R for modelling the data (see Fig. 5). Combining these estimates, we look into the most likely value of  $L'_X$  (SW) and its uncertainty and then assess how probable the reflection-dominated hypothesis might be. Let us label the X-ray and the mid-IR estimates as  $E_i$  ( $i = 0, 1, 2, 3$ ), where E0 is NuSTAR spectral modelling, E1 is 6 $\mu\text{m}$  based, E2: 12 $\mu\text{m}$  based, and E3 is [O iv] based. E0 can be described as  $\log L'_X$  being equally likely between 42.3 and 43.6 [erg s<sup>-1</sup>], or  $E0 \sim \text{Unif}(42.3, 43.6)$ . The mid-IR features based estimates have uncertainties due to scatter around each correlation: 0.4 dex for E1 and 0.23 dex for E2 are given by Mateos et al. (2015) and Gandhi et al. (2009), respectively, and we estimate 0.5 dex for E3. We assume each estimate of  $\log L'_X$  ( $\equiv \mu_i$ ) follows a Gaussian distribution  $E_i \sim N(\mu_i, \sigma_i)$  ( $i = 1, 2, 3$ ):  $E1 \sim N(42.85, 0.5)$ ,  $E2 \sim N(43.17, 0.38)$ ,  $E3 \sim N(43.19, 0.5)$ , where we include a factor of 2 uncertainty of  $f_{\text{AGN}}$  to  $\sigma_1$  and  $\sigma_2$  in addition to the scatter of the correlations. The posterior probability  $\prod E_i$  gives the most likely estimate of  $\log L'_X = 43.13$  (the 95% compatible interval (CI): 42.7–43.6). This is illustrated in Fig. 5. The  $L'_X$  range that can be obtained in SW-A lies below the 95% CI, indicating SW-R to be preferred, and a reflection-dominated spectrum is a more probable description of the NuSTAR data for SW.

Assuming a bolometric correction of 20 (Marconi et al. 2004), the  $L_{\text{AGN}}$  (SW) is found to be  $2.6 \times 10^{44}$  erg s<sup>-1</sup>, based on the best-estimate of  $L'_X$ . The Eddington ratio is then 0.9%, which is typical of Seyferts.  $L_{\text{AGN}}/L_{\text{IR}} \approx 0.3$  can be translated to the AGN fraction in the galaxy's bolometric output if  $L_{\text{AGN}}$  is all absorbed by circumnuclear dust and reradiated in IR.

## 4.2. NE nucleus

The X-ray luminosity of the NE nucleus is relatively low, about  $4 \times 10^{41}$  erg s<sup>-1</sup>. Although the hard Chandra spectrum indicates a

significant AGN contribution in the Chandra band (Torres-Albà et al. 2018), as intense star formation is also taking place in NE, we first examine how much the star-forming activity might contribute to the observed hard X-ray emission. Starburst emission at energies above 3 keV mainly comes from high-mass X-ray binaries. Their collective X-ray luminosity can be estimated using the empirical relation with star formation rate (Grimm et al. 2003; Ranalli et al. 2003; Lehmer et al. 2010). The star formation rate of the whole Mrk 266 system is  $65 M_{\odot} \text{ yr}^{-1}$  (Howell et al. 2010). By scaling with  $L_{\text{IR}}$ , we estimate the star formation rate of NE is  $15 M_{\odot} \text{ yr}^{-1}$ . Using the formula of Lehmer et al. (2010) (given the star formation rate,  $L_X$  is dominated by high-mass X-ray binaries and a contribution of low-mass X-ray binaries is minor), the expected 2–10 keV luminosity from X-ray binaries is found to be  $2.4 \times 10^{40}$  erg s<sup>-1</sup>, or  $\sim 5\%$  of the observed 2–10 keV luminosity. The radial surface brightness profile of NE in the 4–7 keV Chandra image (Fig. 1) shows a small extension ( $\leq 10\%$  of the total emission) which might be attributed to the star formation, but most of the emission comes from a low-luminosity AGN. The 3–7 keV flux observed by Chandra is  $\sim 25\%$  higher than that of XMM-Newton and NuSTAR. Although the increase is marginal, X-ray variability would support the dominance of AGN emission.

The Eddington ratio of NE is rather low ( $\lambda_{\text{Edd}} \sim 2 \times 10^{-4}$ ). Among nearby AGN, the  $\lambda_{\text{Edd}}$  range around this value is populated by LINERs and low-luminosity Seyferts (Ho 2008). Although the radio to mid-IR flux-density ratio,  $q_{24\text{obs}} = \log(S_{1.4\text{GHz}}/S_{24\mu\text{m}}) = 1.1$ , is consistent with those of star-forming galaxies (Sargent et al. 2010), the radio source is compact (unresolved at HPBW =  $0.''3 \times 0.''4$ , Mazzarella et al. 1988) and is likely associated with the AGN, which may have an inefficient accretion flow, suggested by the low  $\lambda_{\text{Edd}}$ , producing the radio emission. The observed radio flux of NE is comparable with that of SW with similar spectral slopes:  $-0.9$  for NE and  $-0.8$  for SW in the 1.4–15 GHz range (Mazzarella et al. 1988), while the intrinsic  $L_X$  is  $\sim 1.6$  dex lower than SW (Table 4). This seems to be compatible to the characteristic radio excess of low-luminosity AGN (LLAGN) with an inefficient accretion flow (Ho 2008).

When the bolometric correction  $\kappa = 16$ , suggested for LLAGN by Ho (2008) is used,  $L_{\text{AGN}} = 6 \times 10^{42}$  erg s<sup>-1</sup> is obtained. The  $L_{\text{AGN}}/L_{\text{IR}}$  is therefore  $\sim 2\%$ . The AGN contribution to the IR luminosity could even be lower if NE has a SED typical of LLAGN which lacks a UV excess, a main source of heating of IR emitting circumnuclear dusts. This is in stark contrast to  $\sim 60\%$  obtained from the mid-IR diagnostics (MIV12). However, the Spitzer IRS spectrum of the NE nucleus alone was taken only from the SL module and lacks the longer wavelength coverage where the key AGN diagnostic lines [Ne v]  $\lambda 14.3$ ,  $24.3\mu\text{m}$  and [O iv]  $\lambda 25.9\mu\text{m}$  are present. This leaves the PAH strengths as the only mid-IR AGN diagnostics that may be biased. Given the low accretion rate inferred from the X-ray observations, strong outflows are expected from the AGN in NE, which fit observed optical and radio signatures pointed out by MIV12. The AGN energy output of NE may be dominated by the mechanical power of those outflowing winds.

## 4.3. Dual AGN in Mrk 266

Mrk 266 exhibits properties that have close relevance to the merger-driven formation of dual AGN and their detectability. Two important characteristics of this merger system are 1) a close nuclear separation of 6 kpc in projection; and 2) the mass ratio of the host spheroids close to unity and thus presumably so the black hole mass ratio. These two are required conditions

for forming dual AGN deduced from cosmological simulations (Steinborn et al. 2016; Volonteri et al. 2016, see also e.g. Hopkins et al. 2006; Solanes et al. 2019). As substantial amount of cold molecular gas ( $\sim$ a few  $10^9 M_{\odot}$ ) is available between the galaxies (Imanishi et al. 2009), this reservoir provides individual galaxies with gas for further accretion, helping the system to evolve into an ULIRG, as argued by MIV12. However, it is interesting to note that the two AGN appear to have distinct characteristics: SW is  $\simeq$  30 times more luminous than NE and they are possibly accreting in different modes as discussed above, suggesting that the accretion conditions might be actually unbalanced between the galaxies. In terms of detectability of dual AGN, heavy obscuration certainly plays a role. Ricci et al. (2017) found an elevated proportion of Compton-thick AGN in advanced mergers with nuclear separations of less than 10 kpc. Mrk 266 fits in the merger stage and the SW nucleus is indeed a Compton-thick AGN which has not been verified until the NuSTAR observation. The spatial resolution of Chandra and the hard X-ray sensitivity of NuSTAR complement each other to identify a Compton-thick AGN in advanced merger systems like Mrk 266 and Mrk 273. A multiwavelength approach, as employed by GOALS, is obviously effective to overcome the obscuration issue (e.g. Hickox & Alexander 2018) which would be naturally expected in luminous merger systems. We refer to an extensive review of both observational and theoretical aspects of dual AGN by De Rosa et al. (2019) where related X-ray observational works on samples selected by various techniques (e.g. Koss et al. 2010, 2012; Comerford et al. 2015; Satyapal et al. 2017) are further discussed.

*Acknowledgements.* This research made use of data obtained from NuSTAR, XMM-Newton and Chandra X-ray Observatory, software packages of HEASoft and R (R Core Team 2017), and the NASA/IPAC Extragalactic Databases (NED), which is funded by the National Aeronautics and Space Administration and operated by the California Institute of Technology. KI acknowledges support by the Spanish MICINN under grant PID2019-105510GB-C33. T.D-S. acknowledges support from the CASSACA and CONICYT fund CAS-CONICYT Call 2018. C.R. acknowledges support from the Fondecyt Iniciacion grant 11190831.

## References

- Armus, L., Mazzarella, J. M., Evans, A. S., et al. 2009, *PASP*, 121, 559  
 Awaki, H., Terashima, Y., Higaki, Y., & Fukazawa, Y. 2009, *PASJ*, 61, S317  
 Baloković, M., Brightman, M., Harrison, F. A., et al. 2018, *ApJ*, 854, 42  
 Bernard-Salas, J., Spoon, H. W. W., Charmandaris, V., et al. 2009, *ApJS*, 184, 230  
 Brassington, N. J., Ponman, T. J., & Read, A. M. 2007, *MNRAS*, 377, 1439  
 Chu, J. K., Sanders, D. B., Larson, K. L., et al. 2017, *ApJS*, 229, 25  
 Comerford, J. M., Pooley, D., Barrows, R. S., et al. 2015, *ApJ*, 806, 219  
 De Rosa, A., Vignali, C., Bogdanović, T., et al. 2019, *New A Rev.*, 86, 101525  
 Diamond-Stanic, A. M., Rieke, G. H., & Rigby, J. R. 2009, *ApJ*, 698, 623  
 Díaz-Santos, T., Armus, L., Charmandaris, V., et al. 2017, *ApJ*, 846, 32  
 Gandhi, P., Horst, H., Smette, A., et al. 2009, *A&A*, 502, 457  
 Grimm, H. J., Gilfanov, M., & Sunyaev, R. 2003, *MNRAS*, 339, 793  
 Gruppioni, C., Berta, S., Spinoglio, L., et al. 2016, *MNRAS*, 458, 4297  
 Hickox, R. C. & Alexander, D. M. 2018, *ARA&A*, 56, 625  
 Ho, L. C. 2008, *ARA&A*, 46, 475  
 Hopkins, P. F., Hernquist, L., Cox, T. J., et al. 2006, *ApJS*, 163, 1  
 Horst, H., Gandhi, P., Smette, A., & Duschl, W. J. 2008, *A&A*, 479, 389  
 Howell, J. H., Armus, L., Mazzarella, J. M., et al. 2010, *ApJ*, 715, 572  
 Hutchings, J. B., Neff, S. G., & van Gorkom, J. H. 1988, *AJ*, 96, 1227  
 Ikeda, S., Awaki, H., & Terashima, Y. 2009, *ApJ*, 692, 608  
 Imanishi, M., Nakanishi, K., Tamura, Y., & Peng, C.-H. 2009, *AJ*, 137, 3581  
 Ishigaki, T., Yoshida, M., Aoki, K., et al. 2000, *PASJ*, 52, 185  
 Iwasawa, K., Mazzarella, J. M., Surace, J. A., et al. 2011, *A&A*, 528, A137  
 Iwasawa, K., U. V., Mazzarella, J. M., et al. 2018, *A&A*, 611, A71  
 Kollatschny, W. & Fricke, K. J. 1984, *A&A*, 135, 171  
 Koss, M., Mushotzky, R., Treister, E., et al. 2012, *ApJ*, 746, L22  
 Koss, M., Mushotzky, R., Veilleux, S., & Winter, L. 2010, *ApJ*, 716, L125  
 Lehmer, B. D., Alexander, D. M., Bauer, F. E., et al. 2010, *ApJ*, 724, 559  
 Liu, T., Wang, J.-X., Yang, H., Zhu, F.-F., & Zhou, Y.-Y. 2014, *ApJ*, 783, 106  
 Liu, W., Veilleux, S., Iwasawa, K., et al. 2019, *ApJ*, 872, 39  
 Lutz, D., Maiolino, R., Spoon, H. W. W., & Moorwood, A. F. M. 2004, *A&A*, 418, 465  
 Madsen, K. K., Grefenstette, B. W., Pike, S., et al. 2020, arXiv e-prints, arXiv:2005.00569  
 Marconi, A. & Hunt, L. K. 2003, *ApJ*, 589, L21  
 Marconi, A., Risaliti, G., Gilli, R., et al. 2004, *MNRAS*, 351, 169  
 Mateos, S., Carrera, F. J., Alonso-Herrero, A., et al. 2015, *MNRAS*, 449, 1422  
 Matt, G., Pompilio, F., & La Franca, F. 1999, *New A*, 4, 191  
 Mazzarella, J. M. & Boroson, T. A. 1993, *ApJS*, 85, 27  
 Mazzarella, J. M., Gaume, R. A., Aller, H. D., & Hughes, P. A. 1988, *ApJ*, 333, 168  
 Mazzarella, J. M., Iwasawa, K., Vavilkin, T., et al. 2012, *AJ*, 144, 125  
 Meléndez, M., Kraemer, S. B., Armentrout, B. K., et al. 2008, *ApJ*, 682, 94  
 Nandra, K. & Pounds, K. A. 1994, *MNRAS*, 268, 405  
 Osterbrock, D. E. & Dahari, O. 1983, *ApJ*, 273, 478  
 Osterbrock, D. E. & Martel, A. 1993, *ApJ*, 414, 552  
 Pereira-Santaella, M., Diamond-Stanic, A. M., Alonso-Herrero, A., & Rieke, G. H. 2010, *ApJ*, 725, 2270  
 R Core Team. 2017, *R: A Language and Environment for Statistical Computing*, R Foundation for Statistical Computing, Vienna, Austria  
 Ranalli, P., Comastri, A., & Setti, G. 2003, *A&A*, 399, 39  
 Ricci, C., Bauer, F. E., Treister, E., et al. 2017, *MNRAS*, 468, 1273  
 Rigby, J. R., Diamond-Stanic, A. M., & Aniano, G. 2009, *ApJ*, 700, 1878  
 Sanders, D. B., Scoville, N. Z., Young, J. S., et al. 1986, *ApJ*, 305, L45  
 Sargent, M. T., Schinnerer, E., Murphy, E., et al. 2010, *ApJS*, 186, 341  
 Satyapal, S., Secrest, N. J., Ricci, C., et al. 2017, *ApJ*, 848, 126  
 Solanes, J. M., Perea, J. D., Valentí-Rojas, G., et al. 2019, *A&A*, 624, A86  
 Steinborn, L. K., Dolag, K., Comerford, J. M., et al. 2016, *MNRAS*, 458, 1013  
 Torres-Albà, N., Iwasawa, K., Díaz-Santos, T., et al. 2018, *A&A*, 620, A140  
 U. V., Medling, A., Sanders, D., et al. 2013, *ApJ*, 775, 115  
 Ueda, Y., Akiyama, M., Hasinger, G., Miyaji, T., & Watson, M. G. 2014, *ApJ*, 786, 104  
 Volonteri, M., Dubois, Y., Pichon, C., & Devriendt, J. 2016, *MNRAS*, 460, 2979  
 Wang, J., Heckman, T. M., Weaver, K. A., & Armus, L. 1997, *ApJ*, 474, 659  
 Wu, H., Zou, Z. L., Xia, X. Y., & Deng, Z. G. 1998, *A&AS*, 127, 521